The Journal of Chemical Physics

AIP Publishing

RESEARCH ARTICLE | DECEMBER 01 2025

Optimal interface structure in anatase–rutile mixed TiO_2 for enhanced charge separation and prolonged carrier lifetime

Special Collection: Annabella Selloni Festschrift

Shi-Meng Gu ; Ye-Fei Li ; Zhi-Pan Liu

J. Chem. Phys. 163, 214701 (2025)
https://doi.org/10.1063/5.0299972

The Journal of Chemical Physics

ARTICLE

pubs.aip.org/aip/jcp

Optimal interface structure in anatase–rutile mixed TiO_2 for enhanced charge separation and prolonged carrier lifetime

Cite as: J. Chem. Phys. 163, 214701 (2025); doi: 10.1063/5.0299972
Submitted: 30 August 2025 • Accepted: 6 November 2025 •
Published Online: 1 December 2025

View Online Export Citation CrossMark

Shi-Meng Gu,[1] **Ye-Fei Li,**[1,a)] **and Zhi-Pan Liu**[1,2,a)]

AFFILIATIONS

[1] State Key Laboratory of Porous Materials for Separation and Conversion, Collaborative Innovation Center of Chemistry for Energy Material, Shanghai Key Laboratory of Molecular Catalysis and Innovative Materials, Key Laboratory of Computational Physical Science, Department of Chemistry, Fudan University, Shanghai 200433, China

[2] State Key Laboratory of Metal Organic Chemistry, Shanghai Institute of Organic Chemistry, Chinese Academy of Sciences, Shanghai 200032, China

Note: This paper is part of the JCP Special Topic, Annabella Selloni Festschrift.

[a)] **Authors to whom correspondence should be addressed:** yefeil@fudan.edu.cn and zpliu@fudan.edu.cn

ABSTRACT

The carrier lifetime in the anatase–rutile mixed TiO_2 spans different time scales in experiments—from values close to those of pure TiO_2 (~1 ns) up to ~20 ns—and correspondingly, photocatalytic activities also vary widely. However, the origin of this variability remains unclear. Here, using our recently developed interface structure prediction method, ML-interface, we identify three atomic-matched interfaces between anatase and rutile. Nonadiabatic molecular dynamics calculations reveal that electron transfer across all three interfaces is rapid, occurring within 33 fs. In contrast, the carrier recombination lifetimes of the interfaces span 1.9–26.2 ns, indicating the importance of interface structures. Notably, the $(114)_{\text{Anatase}}//(2\bar{1}1)_{\text{Rutile}}$ interface exhibits the longest carrier recombination lifetime (~26 ns), thereby benefiting the photocatalytic activity. These findings demonstrate that optimal photocatalytic performance arises from deliberate engineering of interface structures, rather than from simple mixing of anatase and rutile phases.

I. INTRODUCTION

Anatase–rutile mixed TiO_2, such as the well-known P25 (composed of 80% anatase and 20% rutile),[1–3] exhibits higher photocatalytic activity than pure-phase TiO_2 in numerous reactions,[2,4–10] such as water splitting[7,10] and photocatalytic oxidation.[11,12] In mixed-phase TiO_2, the anatase/rutile interface is considered the key active site, as it promotes carrier separation, extends carrier lifetimes, and thereby boosts photocatalytic efficiency.[13,14] However, reported carrier lifetimes in mixed-phase TiO_2 exhibit considerable inconsistencies, ranging from 0.49 to 20 ns,[7,15–24] and the corresponding photocatalytic activities also vary significantly, with some studies showing performance comparable to pure TiO_2,[12,16] while others report up to fourfold enhancements over the single phase.[20,21] The lack of a consistent trend between phase mixing and activity implies that carrier dynamics are not dictated solely by phase composition but are also intricately linked to the atomic structure of the anatase/rutile interface. Therefore, a unified understanding of how interfacial atomic configurations dictate carrier dynamics is highly desirable.

Recent experimental studies have investigated the factors governing charge carrier dynamics in TiO_2-based photocatalysts. Transient absorption spectroscopy (TAS) measurements on pure anatase and rutile films have shown that intrinsic charge recombination times are largely independent of size and porosity for TiO_2 particles.[25,26] In contrast, time-resolved photoluminescence measurements reveal that the presence of the anatase/rutile interface slows the decay of photoluminescence, indicating that photogenerated electrons and holes are efficiently transferred between the two phases rather than recombining radiatively.[16,24,27] Taken together, these findings indicate that it is the atomic structure of the anatase/rutile interface, rather than morphology or particle size, that primarily governs carrier dynamics in mixed-phase TiO_2.[28]

In parallel, several theoretical studies have adopted nonadiabatic molecular dynamics (NAMD) simulations to calculate the lifetime of photogenerated charge carriers. For instance, Wei *et al.*,[29] building upon earlier work by the Deskins group,[30] simulated an anatase(100)//rutile(001) interface and reported an electron–hole recombination lifetime of 6.6 ns, exceeding that of any single-phase TiO_2. Similarly, Wang *et al.*[31] employed the adaptive genetic algorithm (AGA) to model an anatase(101)//rutile(111) heterojunction, predicting a recombination lifetime of ∼150 ns. Li *et al.*[32] constructed an anatase(101)//rutile(110) heterojunction and obtained a recombination lifetime as long as 786 ns. These results clearly demonstrate that the carrier recombination dynamics in TiO_2 are highly sensitive to the atomic-scale interface structure, with different heterojunction orientations leading to variations of several orders of magnitude in the recombination timescale.

In this study, we employed our recently developed interface structure prediction method, ML-interface, to explore the atomic structures between anatase and rutile TiO_2.[33,34] Nonadiabatic molecular dynamics was applied to evaluate carrier recombination dynamics at the anatase/rutile interface. We identified three thermodynamically stable interface orientations: $(114)_A//(2\bar{1}1)_R$, $(110)_A//(01\bar{1})_R$, and $(110)_A//(100)_R$. Among them, the $(114)_A//(2\bar{1}1)_R$ interface exhibited fast electron transfer (∼33 fs) from rutile to anatase and a long non-radiative electron–hole recombination lifetime (∼26 ns), significantly exceeding those of pure anatase or rutile phases. These results provide fundamental atomic-scale insights into how interfacial structures influence charge dynamics in mixed-phase TiO_2.

II. METHODOLOGY

A. Interface structure prediction and stability assessment

The anatase/rutile interface structures are constructed by the ML-interface method, which involves three steps: (i) orientation relationship (OR) screening to identify plausible crystallographic alignments between the two phases, (ii) generation of candidate interface atomic structures using graph-theoretical algorithms to ensure chemically reasonable bonding, and (iii) global optimization based on a global neural network potential to identify low-energy atomic configurations. More details can be found in the supplementary material and our previous literature.[33–35]

The stability of the interface is estimated by the interfacial energy (γ_{int}) using the following equation:

$$\gamma_{\text{int}} = \frac{E(\text{biphase}) - \Sigma_i n_i E_i(\text{pure phase})}{2A}, \tag{1}$$

where $E(\text{biphase})$ is the total energy of the heterojunction, $E_i(\text{pure phase})$ is the energy of a unit cell of the pure phase, n_i is the number of unit cells of the pure phase that make up the heterojunction, and A is the surface area of the heterojunction interface.

B. Nonadiabatic molecular dynamics

The carrier dynamics are calculated using nonadiabatic molecular dynamics[36–38] as implemented in the Hefei-NAMD code,[39] in which classical nuclear trajectories are coupled to quantum electronic states to describe nonadiabatic processes. In this approach, both the nonadiabatic coupling (NAC) and decoherence effects are key factors governing carrier dynamics. NAC determines the strength of electronic transitions along nuclear trajectories and can be explicitly evaluated within the fewest-switches surface hopping (FSSH) framework, which is sufficient to describe electronic evolution in strongly coupled states with large NAC, such as carrier relaxation within a band. Decoherence, which governs the loss of electronic coherence, must be explicitly introduced as a correction to the FSSH dynamics, for example via the decoherence-induced surface hopping (DISH) method, to accurately capture carrier recombination in weakly coupled states.

To be specific, the NAC between states i and j (d_{ij}) is given by[39]

$$d_{ij} = \left\langle \varphi_i \left| \frac{\partial}{\partial t} \right| \varphi_j \right\rangle = \frac{\langle \varphi_i | \nabla_{\mathbf{R}} H | \varphi_j \rangle}{\varepsilon_j - \varepsilon_i} \cdot \dot{\boldsymbol{R}}, \tag{2}$$

where H is the Kohn–Sham Hamiltonian; φ_i and φ_j are the wavefunctions of eigenstates i and j, respectively; ε_i and ε_j are the corresponding energies; and $\dot{\boldsymbol{R}}$ denotes the nuclear velocity. Equation (2) shows that NAC is proportional to the electron–phonon coupling matrix element $\langle \varphi_i | \nabla_{\mathbf{R}} H | \varphi_j \rangle$ and the nuclear velocity $\dot{\boldsymbol{R}}$, while being inversely proportional to the energy difference $\varepsilon_j - \varepsilon_i$.

On the other hand, the decoherence time of carriers is estimated using the pure-dephasing approach, which approximates the full decoherence dynamics based on bandgap fluctuations of the electronic states.[40,41] These fluctuations can be quantified using the unnormalized autocorrelation function (un-ACF),[42]

$$C(t) = \langle \Delta E_g(t) \Delta E_g(0) \rangle, \tag{3}$$

where $\Delta E_g(t) = E_g(t) - \langle E_g \rangle$ is the deviation of the instantaneous bandgap $E_g(t)$ from its canonical average $\langle E_g \rangle$. The pure-dephasing function is obtained via a double integration of the un-ACF,

$$D(t) = \exp\left[-\frac{1}{\hbar^2} \int_0^t \mathrm{d}t_1 \int_0^{t_1} \mathrm{d}t_2 C(t_2) \right]. \tag{4}$$

The pure-dephasing time is then extracted by fitting $D(t)$ to a Gaussian function, $y = \exp\left[-0.5(t/\tau)^2\right]$. The pure-dephasing time and the decoherence time are related by the following equation:

$$\frac{1}{T_2} = \frac{1}{2T_1} + \frac{1}{T_2^*}, \tag{5}$$

where T_2 is the decoherence time, T_1 is the excited-state lifetime, and T_2^* is the pure-dephasing time. Since the excited-state lifetime is much longer than the pure-dephasing time during the carrier recombination, the pure-dephasing time is often used as an approximation for the overall decoherence time. Equation (5) also indicates that the above pure-dephasing approach may slightly overestimate the decoherence time, leading to longer carrier lifetimes.[43]

C. Calculation details

All DFT calculations are performed using the plane wave projector-augmented wave (PAW) method[44] implemented in the Vienna *Ab initio* Simulation Package (VASP) code.[45–47] The Perdew–Burke–Ernzerhof (PBE) functional, combined with the DFT+U approach, is used to treat the strongly correlated 3d electrons of transition-metal elements (U = 3.5 eV for Ti 3d orbitals).[48] A kinetic energy cutoff of 450 eV was employed for the plane wave basis set. Considering the large supercell, only the Γ-point was used for Brillouin zone sampling.

The NAMD simulations were performed using the following setups. The system was first equilibrated at 300 K in the canonical ensemble (NVT) using velocity rescaling. Then, a 5 ps microcanonical (NVE) molecular dynamics trajectory was generated with a time step of 1 fs. The last 3 ps of the NVE trajectory were used as the basis for NAMD simulations. NAMD results were obtained by averaging over 100 distinct initial configurations sampled from the MD trajectory. For each initial configuration, NAMD were simulated by propagating 2×10^4 independent trajectories using the FSSH method for carrier relaxation within bands and 1×10^3 independent trajectories using the DISH method for carrier recombination.

III. RESULTS AND DISCUSSION

A. Geometry and electronic structure

By exploring 2344 likely interface ORs and 52 495 structural minima, we identified three lattice-matched interfaces with strain less than 9% and interfacial energy below 1.7 J/m^2. The identified heterojunction interface structures—$(114)_A//(2\bar{1}1)_R$, $(110)_A//(01\bar{1})_R$, and $(110)_A//(100)_R$ are shown in Fig. 1(a), while the lattice size, strains, and interfacial energies are summarized in Table I. Among them, $(114)_A//(2\bar{1}1)_R$ has the lowest interfacial energy (1.33 J/m^2), followed by $(110)_A//(01\bar{1})_R$ (1.39 J/m^2) and $(110)_A//(100)_R$ (1.65 J/m^2).

The density of states (DOS) for the three interfaces [Fig. 1(b)] shows that all structures exhibit type-II band alignment, where both the conduction band minimum (CBM) and valence band maximum (VBM) of the rutile part lie higher (more positive in energy) than those of the anatase part, without introducing any midgap states. For instance, the $(114)_A//(2\bar{1}1)_R$ interface features a band offset of 0.38 eV for the CBM and 0.30 eV for the VBM, leading to a bandgap of 1.67 eV. Such offsets drive photogenerated electrons to preferentially migrate to anatase while holes accumulate in rutile, consistent with recent experimental observations of electron transfer from rutile to anatase.[21,49,50] The corresponding spatial partial charge densities [Fig. 1(c)] confirm the absence of interface states and reveal well-separated frontier states, with the CBM and VBM localized in the anatase and rutile parts, respectively. For completeness, HSE06 calculations were also performed and yield qualitatively the same conclusions (see Fig. S3 of the supplementary material). Collectively, these features indicate a clean and coherent interface that is favorable for efficient charge-carrier separation.

The structural integrity of the coherent interface can be directly attributed to the atomic arrangements at the interface. In bulk rutile and anatase, Ti atoms are six-coordinated and O atoms are three-coordinated. At the interface, slight relaxation and distortions allow a few Ti atoms to adopt four- or five-coordination and a few O atoms to adopt two-coordination, enabling the lattice to adjust locally without creating dangling bonds or interface states. This atomic-level flexibility accommodates lattice mismatch between the rutile and anatase phases, directly supporting the formation of coherent, defect-free interfaces.

B. Carrier dynamics

In this section, we perform nonadiabatic molecular dynamics simulations to investigate the photoinduced carrier dynamics at the anatase/rutile interfaces. We first focused on carrier relaxation within the conduction and valence bands, using the fewest-switches surface hopping to track the redistribution of photoexcited carriers. Subsequently, the interband (nonradiative) electron–hole recombination across the bandgap is examined using decoherence-induced surface hopping, which accounts for decoherence effects that govern recombination dynamics. Together, both simulations provide a complete picture of carrier relaxation and recombination in the heterostructures.

1. Intraband carrier relaxation and charge separation

The initial location of photoexcited carriers is critical in NAMD simulations, as it directly influences subsequent intraband relaxation pathways and interfacial charge-transfer dynamics. In the anatase/rutile interface, the excited electrons preferentially localize in the rutile region owing to its smaller, direct bandgap compared with anatase.[22,29] Motivated by this property, the initial excited electrons in our NAMD simulations were placed in the lowest-energy conduction-band states localized within the rutile region [CBM+2, CBM+1, and CBM+4 for $(114)_A//(2\bar{1}1)_R$, $(110)_A//(01\bar{1})_R$, and $(110)_A//(100)_R$, respectively].

Starting from this initial excitation setup, we simulate the carrier relaxation of these photoexcited electrons within the conduction band, specifically the CBM+n → CBM transition. In this process, the CBM is delocalized in the anatase region, such that the relaxation of electrons from rutile-localized CBM+n states corresponds to an electron transfer process from rutile to anatase. Figures 2(a)–2(c) present the time evolution of the average energies and orbital populations of the excited electrons. The populations of the higher-energy conduction-band states (dashed blue lines) decay rapidly across all three heterostructures (within 200 fs). By fitting the population decay [Figs. 2(d)–2(f)] using a single-exponential function $P(t) = \exp(-t/\tau)$, the relaxation lifetimes (τ_1) are 33, 27, and 17 fs for $(114)_A//(2\bar{1}1)_R$, $(110)_A//(01\bar{1})_R$, and $(110)_A//(100)_R$, respectively. These results indicate that electrons initially excited in rutile can efficiently transfer across the interface into anatase.

In a similar manner, we simulated the relaxation of holes within the valence band (VBM-n → VBM). Here, the VBM-n states correspond to the highest-energy orbitals localized in rutile [VBM-38, VBM-8, and VBM-21 for $(114)_A//(2\bar{1}1)_R$, $(110)_A//(01\bar{1})_R$, and $(110)_A//(100)_R$, respectively]. The results show that holes also relax efficiently from these higher-energy states to the VBM, with relaxation lifetimes of 10, 15, and 11 fs for the three heterostructures, respectively (see Fig. S4 of the supplementary material). As the relaxed holes occupy the VBM states that are delocalized in rutile, whereas the relaxed electrons reside in the anatase CBM, photogenerated carriers can thus be effectively separated across the interface, with anatase serving as an efficient electron acceptor.

To further understand the physical origin of the fast interfacial carrier transfer dynamics, we analyzed the nonadiabatic couplings (NACs) of the three interfaces, as shown in Fig. 3. The results show that NAC values between electronic states—including both conduction- and valence-band orbitals—are appreciable (∼47–210 meV). For each state, one or two couplings stand out as significantly larger than the others (visible as bright yellow, orange, or purple blocks in each row of Fig. 3), typically arising between energetically adjacent orbitals such as CBM+1 and CBM+2, with magnitudes comparable to those in single-phase TiO_2. These results

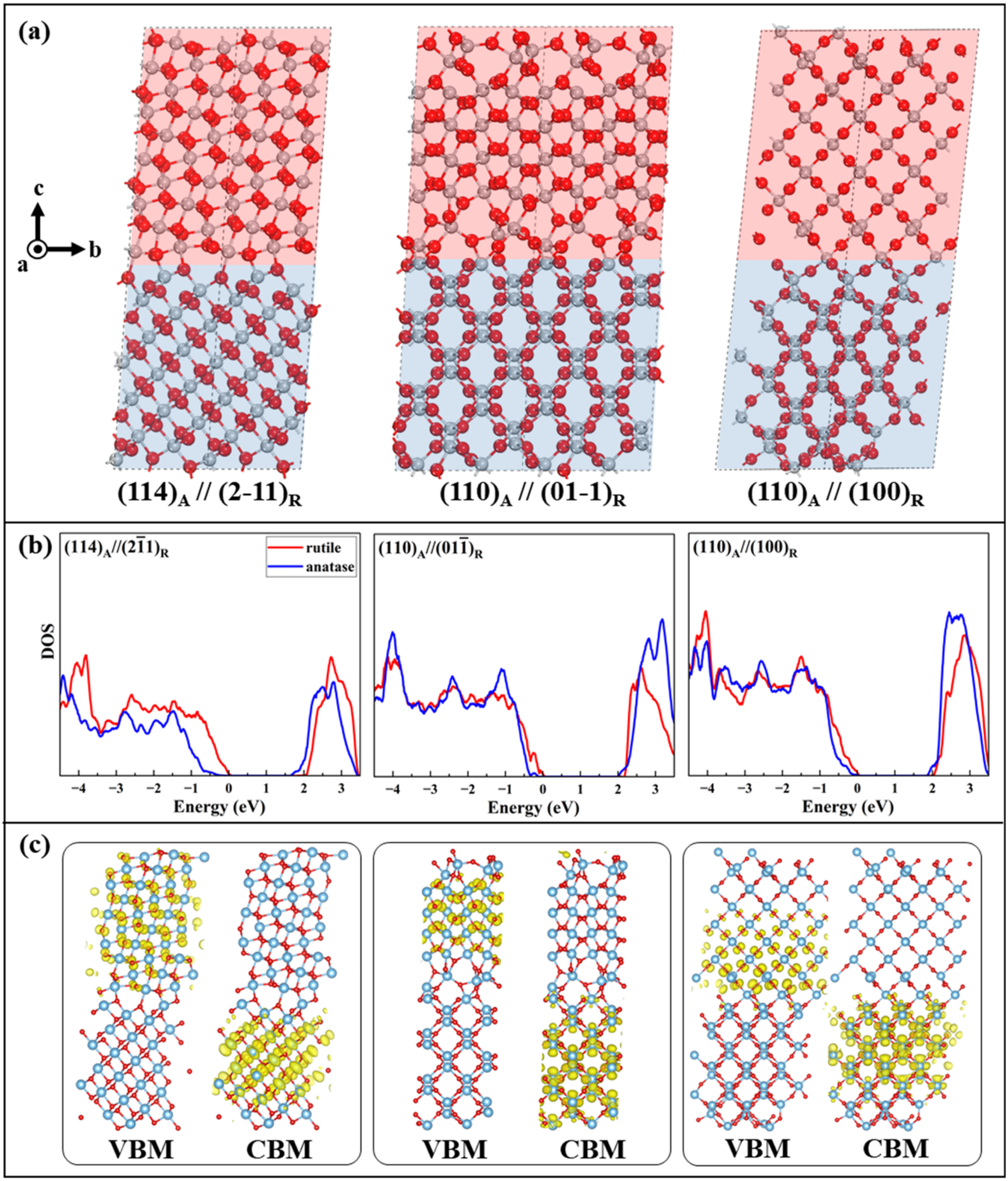

FIG. 1. Structures and electronic structures of anatase–rutile interfaces. Atomic structures (a), density of states (b), and partial charge densities (c) of anatase–rutile interfaces. Gray balls are the Ti atoms and red balls are the O atoms.

TABLE I. Lattice size, strains, interfacial energies, and bandgaps of anatase–rutile interfaces.

Interface	a (Å)	b (Å)	γ (deg)	Thickness[a] (Å)	Number of atoms	Strain (%)	γ_{int} (J/m^2)	Band gap (eV)
$(114)_A//(2\bar{1}1)_R$	11.21	7.42	108.92	33.21	216	6.4	1.33	1.67
$(110)_A//(01\bar{1})_R$	11.10	9.54	89.77	33.15	288	1.8	1.39	2.00
$(110)_A//(100)_R$	11.15	11.09	64.12	37.57	336	8.9	1.65	1.87

[a] Total thickness of the anatase and rutile phases at the interface.

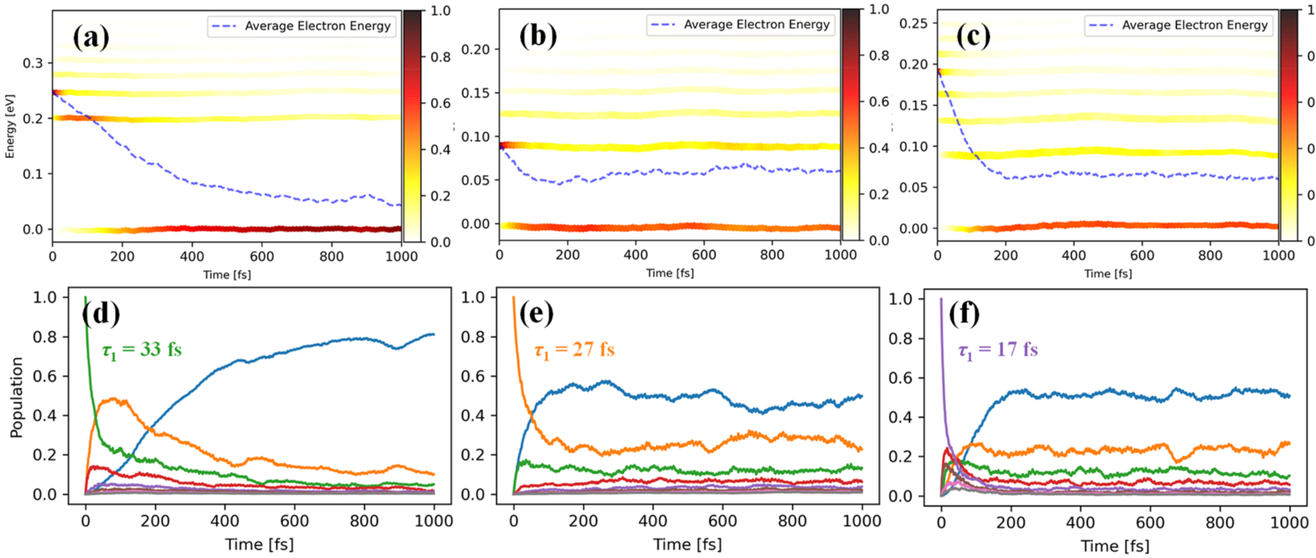

FIG. 2. Decay of excited electrons within the conduction band at anatase–rutile interfaces obtained from NAMD simulations: $(114)_A//(2\bar{1}1)_R$ (left column), $(110)_A//(01\bar{1})_R$ (middle column), and $(110)_A//(100)_R$ (right column). (a)–(c) Time-dependent energy changes for electron transfer. (d)–(f) Time-dependent spatial charge localization of electron transfer. Gray lines: CBM+7, pink lines: CBM+6, brown lines: CBM+5, purple lines: CBM+4, red lines: CBM+3, green lines: CBM+2, orange lines: CBM+1, and blue lines: CBM.

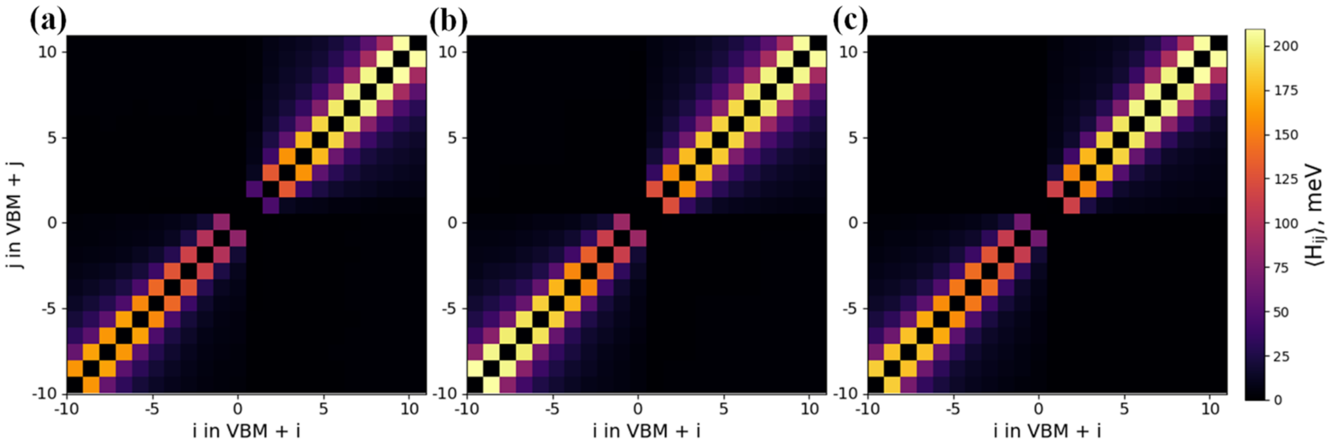

FIG. 3. Average nonadiabatic couplings between states from VBM-10 to CBM+10 along NAMD trajectories: $(114)_A//(2\bar{1}1)_R$ (a), $(110)_A//(01\bar{1})_R$ (b), and $(110)_A//(100)_R$ (c).

indicate that, despite the partial localization of wavefunctions in either rutile or anatase, the interfacial overlap remains significant and provides efficient pathways for carrier separation.

2. Interband carrier recombination

After charge separation, the carriers reside at the interface between the CBM and VBM, with the CBM located in anatase and the VBM in rutile. The recombination rate between the VBM and CBM is, therefore, critical to determining the overall photocatalytic efficiency or quantum yield. To this end, we computed the recombination dynamics using the DISH approach and compared them across the three heterostructures. Figure 4 shows the time evolution of excited-electron populations during electron–hole recombination in the three heterostructures, where the decay of the excited-state population (orange curve) is accompanied by a corresponding increase in the ground-state population (blue curve).

By using single exponential fitting, the carrier recombination lifetimes (τ_2) are 26.2, 6.9, and 1.9 ns for $(114)_{A}//(2\bar{1}1)_{R}$, $(110)_{A}//(01\bar{1})_{R}$, and $(110)_{A}//(100)_{R}$, respectively. In comparison, Table II summarizes the previously reported carrier recombination lifetimes in pure anatase and rutile TiO_2.[29,31,51] $(114)_{A}//(2\bar{1}1)_{R}$ exhibits a significantly prolonged recombination lifetime of 26.2 ns, far exceeding that of either pure anatase or pure rutile. This highlights the effectiveness of its specific interfacial configuration in suppressing electron–hole recombination and thereby enhancing charge separation. $(110)_{A}//(01\bar{1})_{R}$ also shows an extended lifetime (6.9 ns), suggesting moderately improved carrier separation relative to the pure phases. In contrast, $(110)_{A}//(100)_{R}$ displays a much shorter recombination lifetime (1.9 ns), comparable to those observed in pure TiO_2. These results not only fall within the range reported in previous experiments[7,15–22] but also provide a clear structural explanation for the previously observed order-of-magnitude variation in recombination lifetimes, highlighting the decisive role of orientation and atomic structure of the interface in carrier dynamics.

It should be noted that the recombination lifetime can be affected by the size of the supercell. In general, a larger supercell leads to a longer carrier lifetime (and vice versa), as it corresponds to a lower carrier concentration.[52] To further examine this effect, we performed a NAMD simulation on a doubled-size $(114)_{A}//(2\bar{1}1)_{R}$ interface (with 432 atoms), which showed that the recombination lifetime increased from 26.2 to 35.6 ns, consistent with the general trend. Nevertheless, the size effect does not change the order of recombination lifetime at three interfaces. Notably, the $(114)_{A}//(2\bar{1}1)_{R}$ interface with the longest carrier recombination time actually has the smallest supercell among the three interfaces (see Table I). Therefore, scaling the three interfaces to the same size would only result in $(114)_{A}//(2\bar{1}1)_{R}$ having an even longer recombination time than the other two interfaces.

TABLE II. Electron lifetimes in single-phase TiO_2 obtained from NAMD simulations in the literature.

References	Temperature (K)	Lifetime in anatase (ns)	Lifetime in rutile (ns)
29	300	2.27	0.10
31	100	7.5	0.5
	100	⋯	3.92
51	300	⋯	3.11
	700	⋯	0.65

The recombination lifetime can also be influenced by the dissimilar bandgaps estimated by different functionals. For instance, the bandgap of $(114)_{A}//(2\bar{1}1)_{R}$ is 1.67 and 2.47 eV using PBE+U and HSE06, respectively. Accordingly, the NAC calculated using HSE06 is smaller than that obtained using PBE+U [see Eq. (2)], leading to a longer recombination lifetime. Nevertheless, the increase in bandgaps from PBE+U to HSE06 is similar for the three interfaces, with values ranging from 0.80 to 0.88 eV (see Table S1 of the supplementary material). As a result, the reductions in NAC for all three interfaces are comparable, leading to similar extensions of the recombination lifetimes. Altogether, the use of HSE06 does not change the order of recombination lifetimes for the three interfaces.

The significantly extended recombination lifetime of $(114)_{A}//(2\bar{1}1)_{R}$ can be attributed to the combined effects of NAC and electronic decoherence. We first focus on the role of NAC. As summarized in Table III, $(114)_{A}//(2\bar{1}1)_{R}$ exhibits a markedly weaker NAC (0.31 meV), compared with 0.74 meV for $(110)_{A}//(01\bar{1})_{R}$ and 1.06 meV for $(110)_{A}//(100)_{R}$. According to Fermi's golden rule,[53] the recombination rate scales with the square of the NAC magnitude between the involved electronic states, meaning that a smaller NAC directly reduces the recombination probability. This reduction

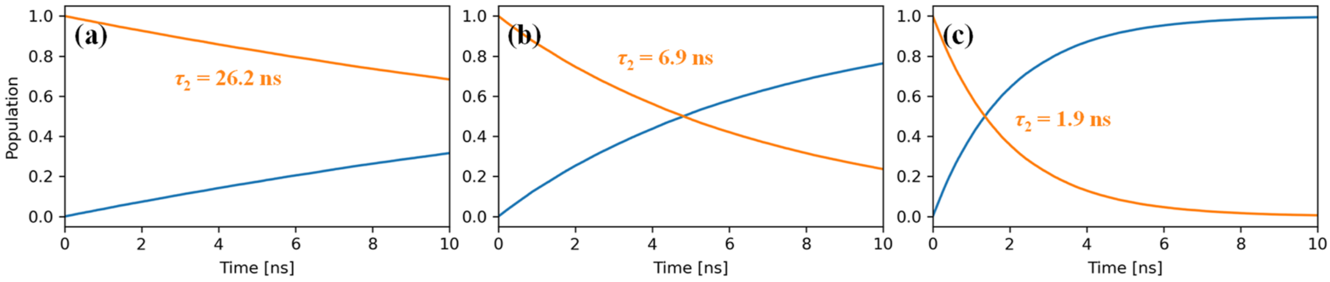

FIG. 4. Nonradiative electron–hole recombination dynamics at the $(114)_{A}//(2\bar{1}1)_{R}$ (a), $(110)_{A}//(01\bar{1})_{R}$ (b), and $(110)_{A}//(100)_{R}$ (c) interfaces. Orange lines represent the time evolution for electron populations in CBM, while blue lines represent the time evolution of electron populations in VBM.

TABLE III. Standard deviation of bandgap, pure-dephasing time, NAC, and carrier recombination lifetime at anatase–rutile interfaces.

Interface	σ_g (eV)	Pure-dephasing time (fs)	NAC (meV)	Carrier recombination lifetime (ns)
$(114)_A//(2\bar{1}1)_R$	0.112	4.37	0.31	26.2
$(110)_A//(01\bar{1})_R$	0.090	5.66	0.74	6.9
$(110)_A//(100)_R$	0.077	6.48	1.06	1.9

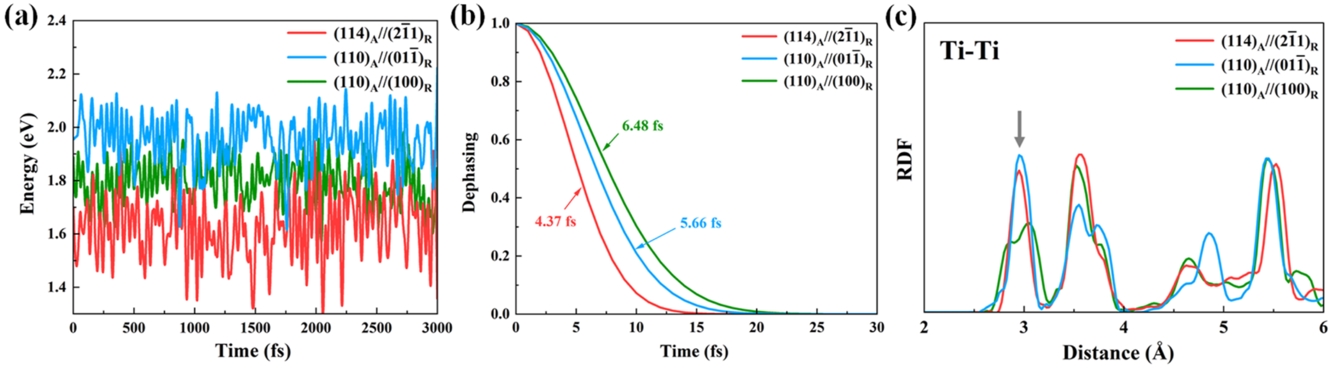

FIG. 5. (a) Time evolution of the bandgaps. (b) Pure-dephasing functions and corresponding pure-dephasing times for the electronic transfer from CBM to VBM. (c) RDF curves of Ti–Ti pairs in anatase–rutile interfaces.

in NAC thus serves as a primary factor underlying the prolonged carrier lifetime at $(114)_A//(2\bar{1}1)_R$ interface.

On the other hand, electronic decoherence also plays a critical role, as rapid loss of coherence can strongly suppress carrier recombination.[54] To quantify this effect, we evaluated the pure-dephasing time of the simulated heterojunctions [see Fig. 5(b)]. These functions capture the temporal decay of quantum coherence between the CBM and VBM states, thereby providing a direct measure of how long electronic superpositions can be sustained during the recombination process. By fitting the dephasing curves with Gaussian functions, we extracted the characteristic decoherence times as 4.37 fs for $(114)_A//(2\bar{1}1)_R$, 5.66 fs for $(110)_A//(01\bar{1})_R$, and 6.48 fs for $(110)_A//(100)_R$, as summarized in Table III. These values reveal distinct coherence lifetimes at the different heterointerfaces, highlighting the sensitivity of carrier dynamics to interfacial atomic structure.

To understand the behavior of the decoherence times, we examined the time-dependent fluctuations of the bandgaps [see Fig. 5(a)], which are known to influence coherence decay: Larger fluctuations generally lead to faster dephasing.[42] The fluctuation amplitude was quantified using the standard deviation (σ_g), defined as

$$\sigma_g = \sqrt{\langle (E_g(t) - \langle E_g \rangle)^2 \rangle}, \tag{6}$$

where $E_g(t)$ denotes the instantaneous energy gap at time t, and $\langle E_g \rangle$ is the canonical average gap energy over the trajectory. As listed in Table III, the calculated σ_g values follow the trend: $(110)_A//(100)_R$ (0.112 eV) > $(110)_A//(01\bar{1})_R$ (0.090 eV) > $(114)_A//(2\bar{1}1)_R$ (0.077 eV). This trend well explains the differences in decoherence times, as faster coherence decay corresponds to larger energy gap fluctuations, consistent with the inverse relationship between σ_g and the dephasing time. Altogether, the combination of a weaker NAC, faster electronic decoherence, and larger energy gap fluctuations of structure $(114)_A//(2\bar{1}1)_R$ jointly suppress carrier recombination, providing a mechanistic explanation for its prolonged lifetime.

In addition to the weak NAC and short pure-dephasing time, it is of interest to understand why the carrier lifetime at $(114)_A//(2\bar{1}1)_R$ interface is particularly long in relation to its interfacial structure. To this end, we analyze the radial distribution functions (RDFs) of the three interfaces [see Fig. 5(c)]. We found that the first-neighbor Ti–Ti peak (centered at 2.9 Å) for the $(114)_A//(2\bar{1}1)_R$ interface exhibits a narrow width compared to the Ti–Ti first-neighbor peaks for the other two interfaces, indicating the $(114)_A//(2\bar{1}1)_R$ interface has the most ordered structure, with less distortion of Ti–O polyhedra. In contrast, the broader peaks observed for the other two interfaces suggest the presence of atomic distortions at the interface. These distortions can perturb the wavefunction, which shortens the carrier recombination time.

IV. CONCLUSIONS

In summary, using the ML-interface method, we identified three energetically stable, atomically matched anatase/rutile interfaces with type-II band alignment. Across these well-matched interfaces, photogenerated carriers can migrate with minimal barrier, enabling ultrafast charge separation within 40 fs, with electrons localized in anatase and holes in rutile. Among them, the

$(114)_A//(2\bar{1}1)_R$ orientation stands out for its low interfacial energy of 1.33 J/m^2 and exceptionally long nonradiative electron–hole recombination lifetime of 26.2 ns, compared with 6.9 ns for $(110)_A//(01\bar{1})_R$ and 1.9 ns for $(110)_A//(100)_R$. This extended lifetime arises from the synergistic effect of weak nonadiabatic coupling (0.31 meV) and short decoherence times (4.37 fs), indicating atomic-scale interface orientation governs both ultrafast carrier separation and prolonged recombination dynamics. Overall, these results demonstrate that high photocatalytic activity requires not only the presence of both anatase and rutile phases but also the deliberate engineering of specific interface orientations to maximize performance.

SUPPLEMENTARY MATERIAL

The supplementary material provides (i) details of the ML-interface method, (ii) electronic structures of the interfaces calculated by the HSE06 functional, and (iii) hole relaxation dynamics within the valence band.

ACKNOWLEDGMENTS

This work received the financial support from the National Science Foundation of China (Grant Nos. 12188101, 22033003, 22122301, and 92472113), the National Key Research and Development Program of China (Grant Nos. 2022YFA1503503 and 2024YFA1509600), the Fundamental Research Funds for the Central Universities (Grant No. 20720220011), the Science & Technology Commission of Shanghai Municipality (Grant No. 2024ZDSYS02), the Natural Science Foundation of Shanghai (Grant No. 24ZR1405100), and the Tencent Foundation for XPLORER PRIZE.

AUTHOR DECLARATIONS

Conflict of Interest

The authors have no conflicts to disclose.

Author Contributions

Shi-Meng Gu: Data curation (equal); Writing – original draft (equal). **Ye-Fei Li**: Conceptualization (equal); Supervision (equal); Writing – review & editing (equal). **Zhi-Pan Liu**: Conceptualization (equal); Funding acquisition (equal); Supervision (equal).

DATA AVAILABILITY

The data that support the findings of this study are available from the corresponding authors upon reasonable request.

REFERENCES

[1] B. Ohtani, O. O. Prieto-Mahaney, D. Li, and R. Abe, J. Photochem. Photobiol., A **216**(2-3), 179–182 (2010).

[2] A. H. Mamaghani, F. Haghighat, and C.-S. Lee, Appl. Catal., B **203**, 247–269 (2017).

[3] Z. Luo, A. S. Poyraz, C.-H. Kuo, R. Miao, Y. Meng, S.-Y. Chen, T. Jiang, C. Wenos, and S. L. Suib, Chem. Mater. **27**(1), 6–17 (2014).

[4] J. Schneider, M. Matsuoka, M. Takeuchi, J. Zhang, Y. Horiuchi, M. Anpo, and D. W. Bahnemann, Chem. Rev. **114**(19), 9919–9986 (2014).

[5] D. C. Hurum, A. G. Agrios, K. A. Gray, T. Rajh, and M. C. Thurnauer, J. Phys. Chem. B **107**, 4545–4549 (2003).

[6] V. G. Bessergenev, M. C. Mateus, A. M. B. do Rego, M. Hantusch, and E. Burkel, Appl. Catal., A **500**, 40–50 (2015).

[7] Y. Liu, X. Zou, L. Li, Z. Shen, Y. Cao, Y. Wang, L. Cui, J. Cheng, Y. Wang, and X. Li, J. Colloid Interface Sci. **599**, 795–804 (2021).

[8] Y. Cho, S. Kim, B. Park, C. L. Lee, J. K. Kim, K. S. Lee, I. Y. Choi, J. K. Kim, K. Zhang, S. H. Oh, and J. H. Park, Nano Lett. **18**(7), 4257–4262 (2018).

[9] Y. Xiao, J. Wu, H. Li, X. Liu, Q. Li, Y. Zhang, and S. Cao, Ceram. Int. **49**(23), 38070–38080 (2023).

[10] F. Cao, J. Xiong, F. Wu, Q. Liu, Z. Shi, Y. Yu, X. Wang, and L. Li, ACS Appl. Mater. Interfaces **8**(19), 12239–12245 (2016).

[11] P. Apopei, C. Catrinescu, C. Teodosiu, and S. Royer, Appl. Catal., B **160-161**, 374–382 (2014).

[12] D. Padayachee, A. S. Mahomed, S. Singh, and H. B. Friedrich, ACS Catal. **10**(3), 2211–2220 (2020).

[13] J. Zhang, Q. Xu, Z. Feng, M. Li, and C. Li, Angew. Chem., Int. Ed. **47**(9), 1766–1769 (2008).

[14] Y. Wu, Y. Chen, D. Li, D. Sajjad, Y. Chen, Y. Sun, S. Liu, J. Shi, and Z. Jiang, Appl. Catal., B **309**, 121261 (2022).

[15] M. Huang, S. Zhang, B. Wu, Y. Wei, X. Yu, Y. Gan, T. Lin, F. Yu, F. Sun, Z. Jiang, and L. Zhong, ACS Catal. **12**(15), 9515–9525 (2022).

[16] X. Ruan, X. Cui, Y. Cui, X. Fan, Z. Li, T. Xie, K. Ba, G. Jia, H. Zhang, L. Zhang, W. Zhang, X. Zhao, J. Leng, S. Jin, D. J. Singh, and W. Zheng, Adv. Energy Mater. **12**(16), 2270066 (2022).

[17] B. Xia, B. He, J. Zhang, L. Li, Y. Zhang, J. Yu, J. Ran, and S. Z. Qiao, Adv. Energy Mater. **12**(46), 2201449 (2022).

[18] M. Liang, X. Shao, J. Y. Choi, Y. D. Kim, T. T. Tran, J. Kim, Y. Hwang, M. G. Kim, Y. Cho, S. Akhtar, and H. Lee, J. Energy Chem. **98**, 714–720 (2024).

[19] L. Liao, Z. Li, J. Lu, Y. Xu, W. Zhou, and Y. Wu, Appl. Catal., B **379**, 125691 (2025).

[20] M. Xu, X. Ruan, M. Z. Shahid, D. Meng, G. Fang, C. Ding, W. Zhang, J. Leng, S. Wang, S. K. Ravi, and X. Cui, Adv. Sci. **12**(12), e2413069 (2025).

[21] J. Qu, J. He, H. Li, Q. Jiang, M. Li, Q. Kong, M. Shi, R. Li, and C. Li, J. Phys. Chem. C **127**(1), 768–775 (2022).

[22] K. Zhang, L. Wang, J. K. Kim, M. Ma, G. Veerappan, C.-L. Lee, K.-j. Kong, H. Lee, and J. H. Park, Energy Environ. Sci. **9**(2), 499–503 (2016).

[23] A. Kafizas, X. Wang, S. R. Pendlebury, P. Barnes, M. Ling, C. Sotelo-Vazquez, R. Quesada-Cabrera, C. Li, I. P. Parkin, and J. R. Durrant, J. Phys. Chem. A **120**(5), 715–723 (2016).

[24] S. Shen, X. Wang, T. Chen, Z. Feng, and C. Li, J. Phys. Chem. C **118**(24), 12661–12668 (2014).

[25] J. Zhang, B. Zhu, L. Zhang, and J. Yu, Chem. Commun. **59**(6), 688–699 (2023).

[26] J. Ma, T. J. Miao, and J. Tang, Chem. Soc. Rev. **51**(14), 5777–5794 (2022).

[27] X. Wang, S. Shen, Z. Feng, and C. Li, Chin. J. Catal. **37**(12), 2059–2068 (2016).

[28] K. Ozawa, S. Yamamoto, R. Yukawa, R. Liu, M. Emori, K. Inoue, T. Higuchi, H. Sakama, K. Mase, and I. Matsuda, J. Phys. Chem. C **120**(51), 29283–29289 (2016).

[29] Y. Wei, M. V. Tokina, A. V. Benderskii, Z. Zhou, R. Long, and O. V. Prezhdo, J. Chem. Phys. **153**(4), 044706 (2020).

[30] J. C. Garcia, M. Nolan, and N. A. Deskins, J. Chem. Phys. **142**(2), 024708 (2015).

[31] Y. Wang, Y. Shi, C. Zhao, Q. Zheng, and J. Zhao, Phys. Rev. B **99**(16), 165309 (2019).

[32] D. Li, R. Li, D. Zhou, X. Qin, and W. Yan, Fuel **388**, 134237 (2025).

[33] Y.-F. Li and Z.-P. Liu, Phys. Rev. Lett. **128**(22), 226102 (2022).

[34] J.-L. Li and Y.-F. Li, J. Mater. Inf. **3**(4) (2023).

[35] J. L. Li, Y. F. Li, and Z. P. Liu, Nat. Commun. **16**(1), 4303 (2025).

[36] C. F. Craig, W. R. Duncan, and O. V. Prezhdo, Phys. Rev. Lett. **95**(16), 163001 (2005).

[37] A. V. Akimov and O. V. Prezhdo, J. Chem. Theory Comput. **9**(11), 4959–4972 (2013).

[38] A. V. Akimov and O. V. Prezhdo, J. Chem. Theory Comput. **10**(2), 789–804 (2014).

[39] Q. Zheng, W. Chu, C. Zhao, L. Zhang, H. Guo, Y. Wang, X. Jiang, and J. Zhao, Wiley Interdiscip. Rev.: Comput. Mol. Sci. **9**(6), e1411 (2019).

[40] S. Mukamel, *Principles of Nonlinear Optical Spectroscopy* (Oxford University Press, New York, 1995).

[41] Z. Zhou, J. Liu, R. Long, L. Li, L. Guo, and O. V. Prezhdo, J. Am. Chem. Soc. **139**(19), 6707–6717 (2017).
[42] A. V. Akimov and O. V. Prezhdo, J. Phys. Chem. Lett. **4**(22), 3857–3864 (2013).
[43] A. B. Madrid, K. Hyeon-Deuk, B. F. Habenicht, and O. V. Prezhdo, ACS Nano **3**(9), 2487–2494 (2009).
[44] G. Kresse and D. Joubert, Phys. Rev. B **59**, 1758 (1999).
[45] G. Kresse and J. Hafner, Phys. Rev. B **48**(17), 13115–13118 (1993).
[46] G. Kresse and J. Hafner, Phys. Rev. B **47**(1), 558–561 (1993).
[47] G. Kresse and J. Hafner, Phys. Rev. B **49**(20), 14251–14269 (1994).
[48] J. P. Perdew, K. Burke, and M. Ernzerhof, Phys. Rev. Lett. **77**, 3865 (1996).
[49] Y. Gao, J. Zhu, H. An, P. Yan, B. Huang, R. Chen, F. Fan, and C. Li, J. Phys. Chem. Lett. **8**(7), 1419–1423 (2017).
[50] D. Shingai, Y. Ide, W. Y. Sohn, and K. Katayama, Phys. Chem. Chem. Phys. **20**(5), 3484–3489 (2018).
[51] L. Zhang, W. Chu, C. Zhao, Q. Zheng, O. V. Prezhdo, and J. Zhao, J. Phys. Chem. Lett. **12**(9), 2191–2198 (2021).
[52] S. Wang, M. Huang, Y. N. Wu, W. Chu, J. Zhao, A. Walsh, X. G. Gong, S. H. Wei, and S. Chen, Nat. Comput. Sci. **2**(8), 486–493 (2022).
[53] O. V. Prezhdo and P. J. Rossky, J. Chem. Phys. **107**(15), 5863–5878 (1997).
[54] S. V. Kilina, A. J. Neukirch, B. F. Habenicht, D. S. Kilin, and O. V. Prezhdo, Phys. Rev. Lett. **110**(18), 180404 (2013).